Open Access

http://pubs.acs.org/journal/acsodf

Article

# Biodegradable Microneedle Patch Confers Crocin with Outstanding Effects in the Treatment of Myocardial Infarction

Qian Liu,[#] Rui Zhao,[#] Danni Zhang,[#] Zhaohuan Lou, Jiangyue Wu, Shiying Hou, Bin Yang, Yunyun Lu, Mengyao Yuan, Shudong Lin, Tianlei Wang, Liang Jin,* and Ling Zhang*

**Cite This:** *ACS Omega* 2025, 10, 14176−14187

Read Online

ACCESS | Metrics & More | Article Recommendations | Supporting Information

**ABSTRACT:** Crocin (CRO), the main active component of *Crocus sativus* (saffron), exhibits significant therapeutic potential for the treatment of myocardial infarction (MI). However, its clinical application is hindered by poor oral administration due to the intestinal barrier. To overcome this limitation, a CRO-incorporated biodegradable microneedle (CRO−DMN) patch was developed to transdermally deliver CRO into the bloodstream, enhancing its therapeutic effect against MI. The microneedle patch, fabricated from sodium hyaluronate (HA), demonstrated excellent mechanical strength, effectively penetrating the stratum corneum and facilitating CRO infiltration to a depth exceeding 300 μm successfully. Studies revealed that CRO was fully released within 30 min postapplication, and the skin self-healed within 90 min after patch removal. Importantly, administration of CRO−DMNs to MI mice resulted in significant improvements in cardiac function and reductions in infarct size compared with CRO treatment alone. Additionally, CRO−DMNs also provided superior protective effects on the myocardium and mitochondria and significantly increased angiogenesis in the infarction border area. In conclusion, CRO−DMNs represent a promising transdermal drug delivery system that effectively improves the therapeutic efficacy of CRO in the treatment of MI.

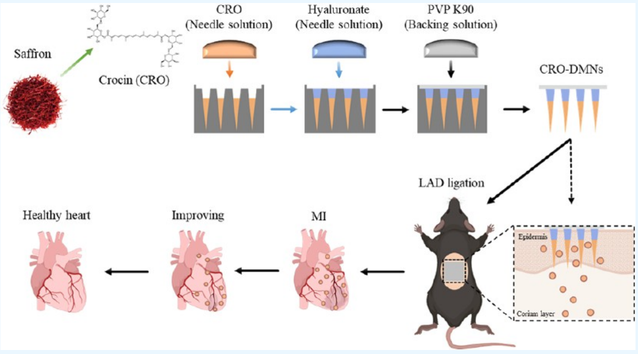

## 1. INTRODUCTION

Myocardial infarction (MI) is a cardiovascular disease with a high mortality rate and has become a serious global health burden.[1] Pathophysiologically, MI is characterized by myocardial necrosis due to insufficient blood supply to cardiomyocytes, essentially a breakdown in the balance of oxygen supply and demand.[2] So far, surgery is still the most common treatment for MI; however, large numbers of postoperative MI survivors are frequently rehospitalized due to refractory myocardial infarction or the development of heart failure. Drug therapy offers advantages such as being painless, noninvasive, and cost-effective. However, few drugs have been shown to effectively and consistently improve MI.[3] Therefore, developing safe and effective pharmacological treatments for MI is imperative.

Medicinal plants have been widely used to prevent and treat many diseases, especially cardiovascular diseases (CVDs).[4] *Crocus sativus*, the dried stigmas of *Crocus sativus* L. belonging to the Iridaceae (iris) family, is the most premium spice in the world and noted as "red gold."[5] It has been an herbal remedy in traditional medicine for various diseases, including CVDs,[6] diabetes,[7] neurodegenerative diseases,[8] metabolic syndrome (MetS),[9] and cancer.[10] Crocin (CRO), a class of water-soluble carotenoids, is one of the major active ingredients of *Crocus sativus*,[11] functioning as an antioxidant,[12] anti-inflammatory,[13] and antiapoptotic[14] agent. It has been utilized in the treatment of Alzheimer's disease,[15] depression,[16] lung injury,[17] atherosclerosis,[18] and more. Previous studies have shown that CRO reduces infarct size and ameliorates MI-induced cardiac impairment, possibly related to its antioxidant, anti-inflammatory, and antiapoptotic properties, indicating its potential as a cardioprotective candidate.[19−21] However, its application is limited due to rapid hydrolysis in the intestine after oral administration,[22−24] preventing its absorption into the bloodstream to exert therapeutic effects. Hence, despite its advantageous effects, the chemical instability of CRO poses a hurdle to its therapeutic application, and there is a pressing need for an innovative drug delivery system that can facilitate direct administration of CRO into the bloodstream, thereby circumventing potential hydrolysis.

**Received:** December 23, 2024
**Revised:** February 6, 2025
**Accepted:** February 14, 2025
**Published:** February 20, 2025

https://doi.org/10.1021/acsomega.4c11540

Transdermal drug delivery systems (TDDs) represent a promising avenue for drug administration, offering a noninvasive approach that addresses the limitations associated with conventional delivery methods. Oral drugs often face degradation in the gastrointestinal tract, while injectable drugs can be associated with discomfort and inconvenience. However, the physiological barrier of the skin hinders the delivery efficiency of traditional patches. Microneedle technology, a third-generation transdermal drug delivery system, overcomes the physical barriers of the skin.[25] Microneedles enable drug delivery through a series of micron-sized, finely tipped needles that penetrate the stratum corneum (SC) of the skin to create microchannels, effectively minimizing pain and tissue damage.[26] In recent years, there has been a rapid rise in the application of microneedles in the fields of wound healing,[27,28] disease treatment,[29−31] bioassays,[32,33] and vaccine delivery.[34] Dissolving microneedles (DMNs) are a specific type of microneedles composed of water-soluble polymers or biodegradable materials that undergo dissolution within the skin microenvironment following skin puncture, thereby obviating concerns regarding needle breakage and ensuring optimal biocompatibility.[35] Hyaluronic acid (HA), a naturally occurring component in the human body, has been identified as a potential candidate for DMN-based drug delivery systems due to its excellent biocompatibility and sufficient strength to puncture the skin.[36] Therefore, HA was used as the matrix material to build a CRO-incorporated dissolving microneedle patch (CRO−DMN).

In this study, we present a new CRO−DMN drug delivery system and evaluate its therapeutic effect on myocardial infarction. We systematically characterize the morphology, mechanical properties, skin penetration ability, *in vivo* dissolution, *in vitro* drug release, and drug loading of the CRO−DMNs. Our findings demonstrate that CRO−DMNs enable the safe entry of CRO into the circulatory system while effectively restoring cardiac function, promoting neovascularization, and inhibiting collagen formation in mice with MI. These results indicate that CRO−DMNs are a safe and effective approach for treating MI.

## 2. EXPERIMENTAL SECTION

**2.1. Preparation of DMNs and CRO−DMNs.** To fabricate DMNs, HA powder (MW ∼ 8000−15,000 Da, Aladdin, Shanghai, China) was dissolved in deionized water to prepare a 15% (w/v) HA solution, serving as the tip solution. This solution was thoroughly mixed and left at 4 °C overnight to ensure complete dissolution. Subsequently, the tip solution was introduced into the polydimethylsiloxane (PDMS) molds (pyramid-shaped, 20 × 20 array; height: 600 $\mu$m; base width: 290 $\mu$m; needle spacing: 800 $\mu$m; Guangzhou Shiling Laker Mold Co.) and centrifuged at 4000 rpm for 40 min at 4 °C in a centrifuge (Eppendorf 5810R, Germany) to fully fill the PDMS mold cavities. After centrifugation, any excess solution on the mold surface was carefully scraped off, and the assembly was dried in a dryer for 2 h. This process was repeated under identical conditions to refill the mold with the 15% HA solution, ensuring the complete formation of the needle tips. Next, a PVP-K90 solution (10%, w/v, Aladdin, Shanghai, China) was applied as the backing layer onto the mold. The centrifugation steps were repeated to ensure a firm bond between the needle tips and the backing layers, followed by drying the mold in the dryer. After drying, the DMNs were carefully detached from the PDMS mold.

For the fabrication of CRO−DMNs, a specified quantity of CRO was dissolved in 15% (w/v) HA solution to achieve a final concentration of 2 mg/mL. The subsequent fabrication steps were identical to those employed for the preparation of DMNs.

**2.2. Mechanical Strength.** First, the DMNs or CRO−DMNs were subjected to the weight-bearing change experiment using weights. DMNs or CRO−DMNs were placed on a horizontal table, and weights were pressed on top of them and kept for 10 s. After the removal of the weights, the deformation of the microneedles was observed under a microscope. The weight of the weights was gradually increased, and the morphology of the microneedles under different loads was examined to investigate their weight-bearing capacity. The compression test was performed on DMNs or CRO−DMNs using a TA.XT Plus Texture Analyzer (Stable Micro Systems, United Kingdom). Cylindrical probes with a diameter of 2 mm were mounted in the test. After the height was calibrated, the distance between the probe and the base was set to a constant value. Samples of 2 × 2 DMNs or CRO−DMNs were carefully cut and placed on the stainless steel base with the microneedle tips pointing upward. The probe was then pressed vertically downward against the microneedles at a constant rate of 0.1 mm/s. The trigger force was set at 0.05 N. Upon contact between the probe and the microneedle tips, force values were recorded until a preset strain of 50% was reached.

**2.3. *In Vivo* Insertion.** Male C57BL/6 mice (6−7 weeks old) were obtained from Zhejiang Chinese Medical University. All experiments were conducted in accordance with the Guide for the Care and Use of Laboratory Animals published by the United States National Institutes of Health (NIH Publication No. 85-23, revised 1996) and were approved by the university's Animal Ethical and Welfare Committee (Approval No. IACUC-20210927-12). Mice were maintained under standard conditions at 23 °C with 60% relative humidity and had free access to food and water. To evaluate the puncture characteristics of DMNs and CRO−DMNs, as well as the changes in skin barrier function after microneedles perforation, transepidermal water loss (TEWL) measurements were performed using the Vapometer SWL5 (Delfin Technologies Ltd., Finland). The dorsal skin of the mice was shaved 24 h prior to the experiment to ensure that the stratum corneum remained intact. TEWL values were measured for two groups: (1) intact skin sites without DMNs or CRO−DMNs treatment and (2) skin sites after the application and removal of DMNs or CRO−DMNs. The probe was gently placed in contact with the designated skin site using constant pressure until stable readings were obtained. TEWL values were collected at specific time points: 15 min before treatment and 0, 15, 30, 60, and 90 min after treatment for each group.

**2.4. *In Vivo* Degradation.** The *in vivo* degradation of DMNs or CRO−DMNs was studied by using mice. DMNs or CRO−DMNs were applied to the shaved dorsal skin of the mice and secured with medical tape. After 90 min, the patches were removed. The residual DMNs or CRO−DMNs were observed under a microscope (s-20L, Motic, China) to assess their degradation *in vivo*.

**2.5. Skin Healing and Skin Irritation.** To evaluate skin healing and potential skin irritation, DMNs or CRO−DMNs were applied to the dorsal skin of anesthetized mice for 30 s and then removed. The application sites were regularly monitored using a camera to document the healing process and any signs of skin irritation.

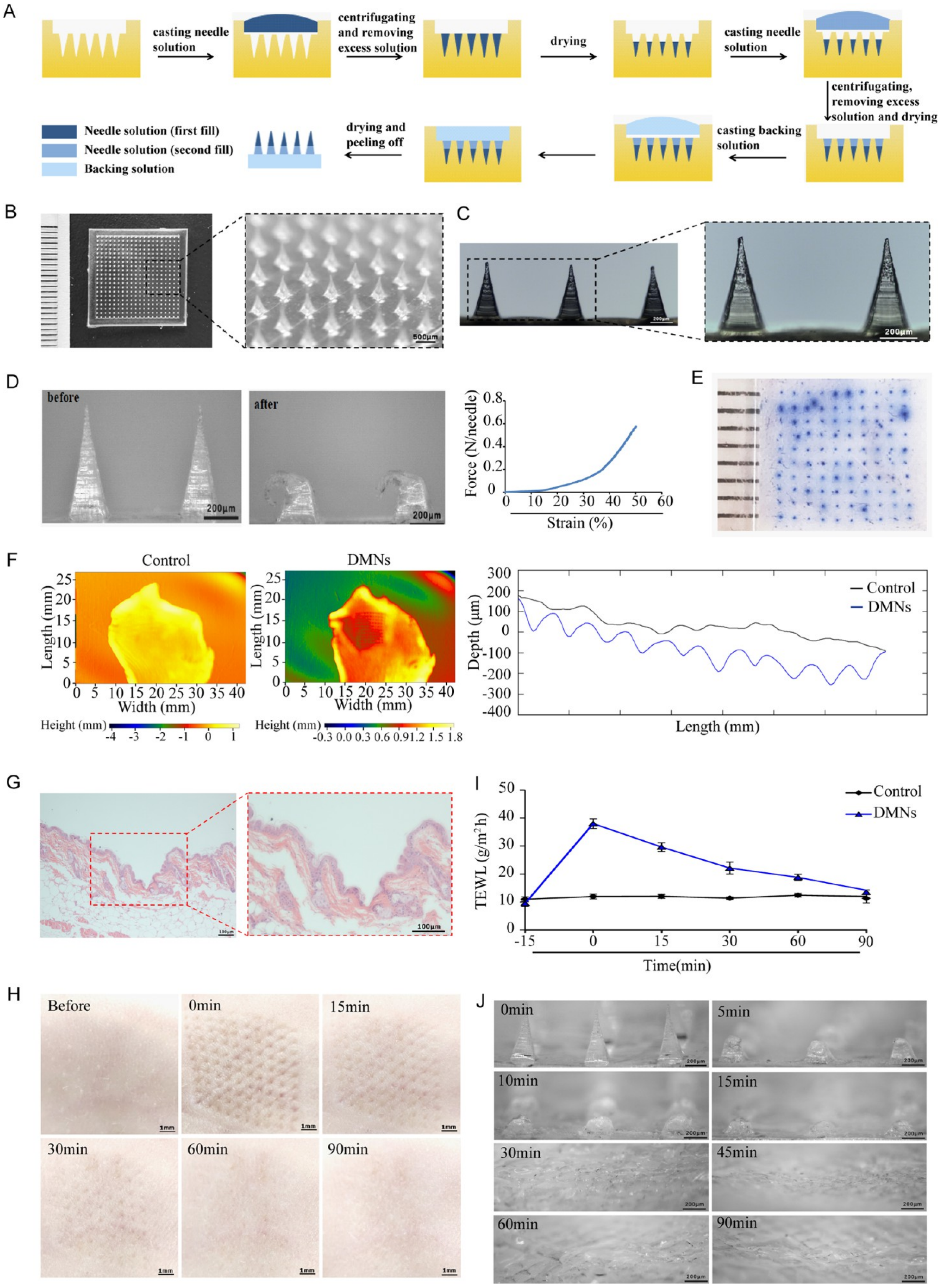

**Figure 1.** Preparation and characterization of DMNs. (A) Schematic diagram of a three-step method for fabricating DMNs. (B) Full view and partial enlargement of DMNs (Bar = 500 $\mu$m). (C) Representative bright-field microscopy images of DMNs (Bar = 200 $\mu$m). (D) Quantitative mechanical properties of the needles detected using a physical property analyzer with the stress−strain curve displayed. (E) *In vitro* skin experiment showing trypan blue staining to demonstrate skin puncture by DMNs. (F) Height of the skin cross section before and after DMN processing detected by PRIMOS, with automatically generated contour lines. (G) Penetration depth of DMNs into the skin as revealed by HE staining. (H) Optical microscopy images of DMNs from a side view before and after insertion into the back of mice *in vivo* (Bar = 1 mm). (I) TEWL values representing skin water loss measured before, immediately after, and at 15, 30, 60, and 90 min after DMN treatment ($n$ = 3). (J) *In vivo* degradation process of DMNs observed by optical microscopy at various time intervals after insertion (Bar = 200 $\mu$m).

**2.6. *In Vitro* Insertion.** The penetration ability of DMNs or CRO−DMNs was further evaluated using the phase shift rapid *in vivo* measurement of the skin (PRIMOS; GFM, Germany) device to analyze microscopic skin morphology before and after treatment. The device projects digital streaks onto the skin, and an equipped camera captures changes in the stripe light to record height differences in the measurement area. We examined the same area of isolated mice skin before and after treatment with DMNs or CRO−DMNs using PRIMOS to obtain and evaluate the skin surface profiles and height differences using PRIMOS software, version 5.7.

Parafilms (PFs) were used as skin simulants to test the penetration depth of DMNs or CRO−DMNs. Seven layers of PFs were stacked to simulate different skin thicknesses. The DMNs or CRO−DMNs were inserted vertically into the PFs for 30 s and then withdrawn. The layers of the PFs were observed under a stereomicroscope, and the penetration depth was estimated based on the number of layers pierced.

The skin insertion rate of DMNs or CRO−DMNs was also examined by using trypan blue staining (Beyotime, Shanghai, China). DMNs or CRO−DMNs were pressed vertically into isolated mouse skin tissue for 30 s and then removed. The puncture site was exposed to trypan blue solution (0.4%, w/w) for 30 min. Residual dye on the skin surface was washed off with alcohol, and the punctured skin area was observed by using a stereomicroscope (Motic, China). Successful penetration by the DMNs or CRO−DMNs was indicated by the appearance of small blue dots within the skin.

**2.7. *In Vitro* Release.** To assess the *in vitro* release of CRO from the CRO−DMNs, a single layer of PF was placed on a foam plate. The CRO−DMNs were inserted into this PF layer and held in place for 30 s to ensure proper microneedle tip exposure. The PF was folded around the base plate of the CRO−DMNs and sealed, forming a closed "bag" configuration. Release experiments were conducted by floating the sealed PF/CRO−DMN array system in a beaker containing deionized water maintained at 37 °C in a constant temperature bath. The solution was stirred at a constant rate to simulate the physiological conditions. At predetermined time intervals, samples were extracted from the beaker, and an equal volume of fresh deionized water was added to maintain a constant volume. The collected samples were subsequently analyzed for CRO content using high-performance liquid chromatography (HPLC) (Agilent).

**2.8. MI Induction and Treatment.** Male C57BL/6 mice (6−7 weeks) were obtained from Zhejiang Chinese Medical University. All experiments were conducted in accordance with the Guide for the Care and Use of Laboratory Animals published by the United States National Institutes of Health (NIH Publication No. 85-23, revised 1996) and were approved by the university's Animal Ethical and Welfare Committee (Approval No. IACUC-20210927-12). The mice were maintained at 23 °C with 60% relative humidity and had free access to food and water. The mice received the left anterior descending coronary artery (LAD) permanently ligated after pentobarbital (50 mg/kg, ip) anesthesia to produce myocardial infarction. The sham-operated group underwent the same thoracotomy procedure without LAD ligation. Low doses of CRO−DMNs treatment (2 mg/kg, L-CRO+DMNs), high doses of CRO−DMNs treatment (10 mg/kg, H-CRO+DMNs), CRO treatment (2 mg/kg, i.v.), DMNs only (DMNs), or saline alone (MI) were administered 28 days after operation.

**2.9. Echocardiography.** Six groups of mice (Sham, MI, DMNs, L-CRO+DMNs, H-CRO+DMNs, and CRO) were subjected to echocardiographic measurements immediately after MI (post) and 28 days after MI. Mice were anesthetized via inhalation of 1.5−2% isoflurane. M-mode tracking (Vevo 2100 Imaging System, VisualSonics, Inc.) was recorded at the level of the papillary muscle through the anterior and posterior ventricular (LV) walls. The cardiac functional parameter, ejection fraction (EF), was calculated to evaluate the heart function.

**2.10. Histological Analysis.** Hearts from all 6 groups of mice were harvested 28 days after myocardial infarction induction and fixed in 10% formaldehyde buffer for paraffin sectioning (5 μm). The Masson's trichrome staining was performed using a Masson's trichrome staining kit (Solaribio, Beijing, China) to evaluate the infarct area. The images were measured using the Image-Pro Plus (Media Cybernetics). The infarct area was measured as the ratio (%) of the injured area to the entire left ventricular area. Haematoxylin and eosin (HE) staining was conducted to assess histopathological changes, and the stained heart sections were examined and photographed under a microscope.

For immunostaining of α-smooth muscle actin (α-SMA)/CD31, heart tissue sections were fixed in 4% paraformaldehyde, permeabilized with 0.2% Triton X-100 (Aladdin, Shanghai, China), and blocked with phosphate-buffered saline containing 0.1% Tween-20 (PBST) containing 5% bovine serum albumin (BSA). Samples were incubated with anti-α-SMA antibody (Cell Signaling Technology, Boston) and anti-CD31 antibody (Cell Signaling Technology, Boston) at 4 °C overnight. After several washes with PBST, the samples were incubated with fluorescently labeled secondary antibodies for 1 h at room temperature. Nuclei were stained with DAPI (Beyotime, Shanghai, China) 1 μg/mL. Fluorescence images were obtained from 4 to 5 randomly selected views in the border area of the ischemic myocardium, and the mean number of microvessels per field was calculated using fluorescence microscopy (Olympus, Japan).

**2.11. Transmission Electron Microscopy.** Heart tissue samples were fixed with 2.5% glutaraldehyde (Aladdin, Shanghai, China) in phosphate-buffered saline (PBS) overnight at 4 °C, dehydrated in graded ethanol solution, and then embedded and sectioned. Observations were made with transmission electron microscopy (JEOL, Japan).

**2.12. Statistical Analysis.** All values were presented as mean ± standard deviation. Statistical analysis with one tailed *t* tests for comparisons between two groups and one-way analysis of variance for comparisons among more than two groups and $p < 0.05$ was considered statistically significant.

## 3. RESULTS

**3.1. Preparation and Characterization of Dissolving Microneedles (DMNs).** DMNs were fabricated using a three-step process. Briefly, a 15% (w/v) HA solution served as the tip solution and was added to the PDMS mold twice to ensure complete filling of the needle cavities, and then a 10% (w/v) PVP-K90 solution was used as the backing solution to fill any gap at the base of the needle from the first two steps (Figure 1A). The resulting DMNs comprised a 20 × 20 array of 400 pyramidal microneedles, each measuring approximately 550 μm in height (Figure 1B,1C). DMNs exhibited a uniform shape and size with excellent structure integrity, showing no evidence of needle breakage.

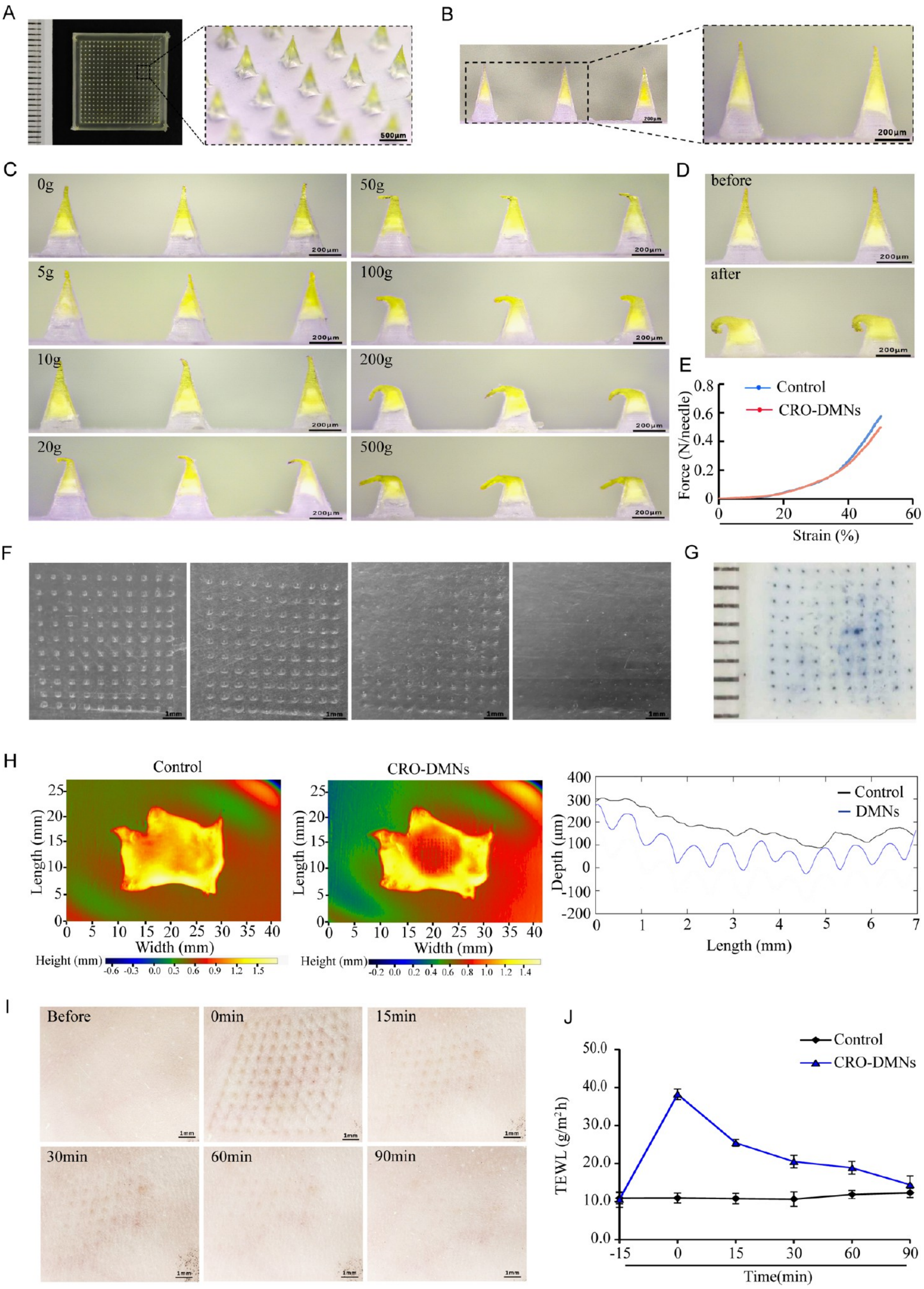

**Figure 2.** Preparation and characterization of CRO−DMNs. (A) Full view and partial enlargement of CRO−DMNs (Bar = 500 $\mu$m). (B) Representative bright-field microscopy images of CRO−DMNs (Bar = 200 $\mu$m). (C) Morphological changes of CRO−DMNs (3 × 3 array) under different applied weights. (D) Quantitative mechanical properties of the needles detected using a physical property analyzer. (E) Stress−strain curve of CRO−DMNs. (F) Optical microscope images of different PF layers after insertion test using CRO−DMNs. (G) *In vitro* skin experiment showing trypan blue staining to demonstrate skin puncture by CRO−DMNs. (H) Height of the skin cross section before and after CRO−DMNs processing was detected by PRIMOS, with automatically generated contour lines. (I) Optical microscopy images of CRO−DMNs from a side view before and after insertion into the back of mice *in vivo* (Bar = 1 mm). (J) TEWL values representing skin water loss measured before, immediately after, and at 15, 30, 60, and 90 min after CRO−DMNs treatment ($n$ = 3).

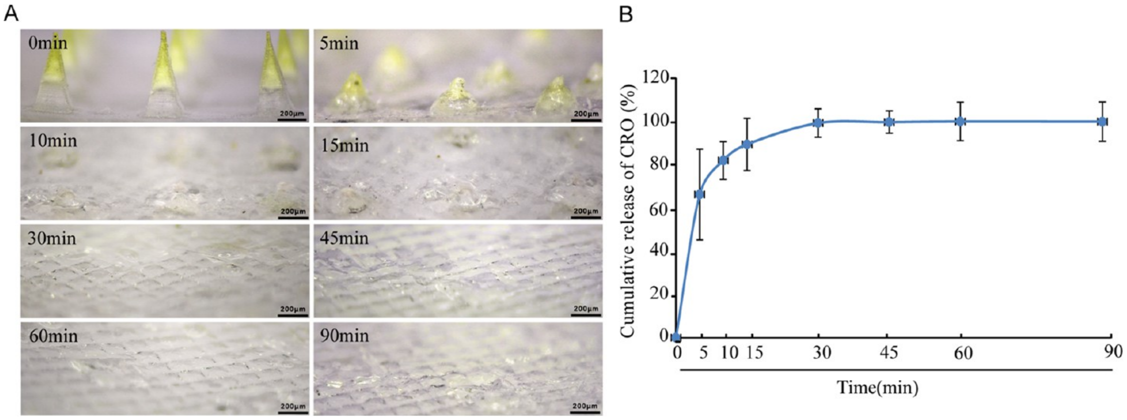

**Figure 3.** Crocin release from CRO−DMNs. (A) Optical microscopy images of CRO−DMNs from a side view before and after insertion into the back of mice *in vivo*. (B) *In vitro* crocin release profiles from CRO−DMNs over time ($n = 8$).

To assess whether DMNs possess sufficient mechanical strength to penetrate the skin barrier for drug delivery, weight-bearing tests were performed by applying varying weights to the DMNs. As the applied weight increased, DMNs displayed gradual bending but maintained structural integrity, withstanding a maximum load of 500 g without fracturing (Supplementary Figure 1A). Further quantitative analysis of mechanical properties was performed using compression tests with a physical property analyzer, and the corresponding stress−strain curve was presented in Figure 1D. The results indicated that the DMN patch could withstand a pressure of 5.7 N per needle at 50% compression deformation, surpassing the minimum force required for effective skin penetration, which is approximately 0.058 N per needle.[37,38] Of note, DMNs maintained their structural integrity throughout the stressing process without any signs of breaking or fracturing (Figure 1D).

The penetration performance of DMNs was evaluated using PF as a skin simulant.[39] The DMNs successfully penetrated three layers of PFs and reached the fourth layer, with insertion depths ranging from approximately 432 to 576 $\mu$m, as measured by vernier calipers (Supplementary Figure 1B). This suggests that DMNs could deliver drugs effectively to the dermis layer. The above result was further confirmed through *in vitro* skin experiment. As shown in Figure 1E, trypan blue staining revealed a well-organized arrangement of blue dots at the DMN insertion sites, indicating a 100% penetration rate. This observation suggests that DMNs successfully penetrated the stratum corneum and reached the dermis layer. Further validation was obtained using PRIMOS and histopathological analysis of the skin samples. The contour lines automatically generated by PRIMOS provided a detailed profile of skin height differences before and after DMN application. As shown in Figure 1F, DMN treated skin exhibited 10 significant depressions compared to untreated skin, indicating successful skin penetration. In addition, HE staining showed that the penetration depth of DMNs was 266 ± 7 $\mu$m, confirming that DMNs reached the dermis without damaging nerves or capillaries (Figure 1G).

Then, skin healing evaluation of DMNs was conducted on mice *in vivo*. As shown in Figure 1H, pinholes on the skin surface were clearly visible immediately after DMN insertion but became indiscernible after 90 min. Furthermore, no signs of edema, erythema, or infection were observed at the treatment sites, indicating negligible skin irritation. In addition, the transepidermal water loss (TEWL) values, which indicated the amount of water lost from the skin, were measured before treatment, immediately after treatment, and at 15, 30, 60, and 90 min post-treatment. The TEWL value of intact skin was 10.8 ± 1.1 $g/m^2 \cdot h$ before DMN treatment. Immediately after treatment with DMNs, the TEWL value increased to 39.0 ± 1.7 $g/m^2 \cdot h$, then gradually decreased to baseline levels within 90 min, suggesting complete healing of the microchannels caused by DMNs (Figure 1I).

Finally, we observed the *in vivo* degradation of DMNs 0, 5, 10, 15, 30, 45, 60, and 90 min after their insertion into the skin. Initially, DMNs displayed a distinct and intact pyramidal shape. Upon insertion, gradual degradation of the tips occurred due to its absorption by the skin within a span of 30 min (Figure 1J).

### 3.2. Preparation and Characteristics of CRO−DMNs.

CRO−DMNs were prepared by a slightly modified three-step approach similar to that described previously. In this variation, the HA solution was supplemented with 2 mg/mL crocin (CRO) and subsequently employed to fill the mold cavities, compensating for water evaporation during drying. The resulting CRO−DMNs formed a 20 × 20 array of pyramid microneedles, each approximately 550 $\mu$m in height, with CRO concentrated in the needle shaft as shown in Figure 2A,2B.

The mechanical properties of CRO−DMNs were assessed under increasing loads. CRO−DMNs exhibited gradual flexure with increasing weight, and under a 500 g load, they displayed significant bending without fracturing (Figure 2C). The stress−strain curve showed that CRO−DMNs could withstand a pressure of 5.0 N per needle at 50% compression deformation (Figure 2D,2E), comparable to the DMNs without CRO. This indicates that the incorporation of CRO did not compromise the mechanical strength of the microneedles.

Similar to DMNs, CRO−DMNs successfully penetrated three layers of the PFs and contacted the fourth layer (Figure 2F). Trypan blue staining showed that CRO−DMNs effectively penetrated the stratum corneum and reached the dermis in skin samples (Figure 2G). The PRIMOS was utilized to detect changes in skin cross section height before and after CRO−DMNs application. As shown in Figure 2H, the contour lines were smooth prior to CRO−DMNs treatment, while post-treatment contours displayed up to 10 significant depressions, indicating successful insertion of CRO−DMNs into the skin.

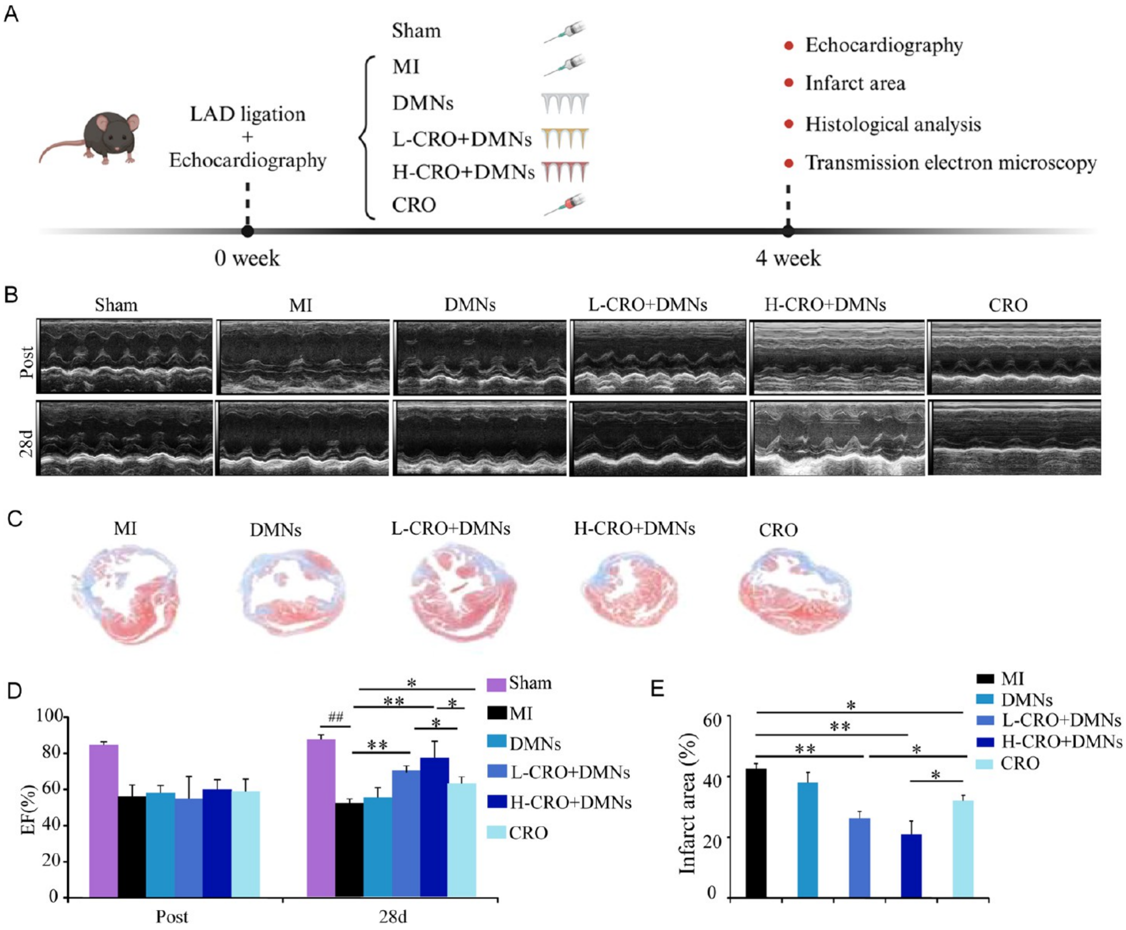

**Figure 4.** CRO−DMNs improved cardiac function and reduced the infarct size in post-MI hearts. (A) Schematic diagram of the *in vivo* experimental design created with BioRender.com. After inducing MI model via LAD coronary artery ligation, mice were randomly divided into six groups: Sham (without LAD ligation, saline, i.v.), MI (saline, i.v.), DMNs (microneedles without CRO), L-CRO+DMNs (DMNs with 2 mg/kg CRO), H-CRO+DMNs (DMNs with 10 mg/kg CRO), and CRO (2 mg/kg, i.v.). Echocardiography was performed immediately after MI induction. Four weeks later, assessments including echocardiography, myocardial infarction area evaluation, histological examination, and transmission electron microscopy were performed. (B) Representative cardiac ultrasound images for each group immediately after MI (Post) and 28 days after MI (28d). (C) Masson's trichrome stained images of heart sections from each group at 28 days after MI. (D) Statistical analysis of EF for each group at 28 days after MI. (E) Quantification of the infarct area (%) based on Masson's trichrome stained images. All data are presented as means ± SD $n \geq 6$ (number of animals/group), $*P < 0.05$, $**P < 0.01$ compared with the MI group or CRO group; $\#\#P < 0.01$ compared with the Sham group.

*In vivo* skin healing evaluation showed that the pinholes on the skin surface caused by CRO−DMNs disappeared within 90 min (Figure 2I). TEWL measurements indicated that the mean TEWL values of intact skin were consistent among groups ($14.8 \pm 4.0$ g/m$^2$·h). Immediately after CRO−DMNs insertion, the mean TEWL value significantly increased to $87.0 \pm 3.5$ g/m$^2$·h, followed by a gradual restoration to the normal level within 90 min, indicating minimal skin damage and efficient recovery (Figure 2J).

**3.3. Evaluation of Degradation of CRO−DMNs and Release Level of Crocin.** The *in vitro* degradation of CRO−DMNs was monitored at 0, 5, 10, 15, 30, 45, 60, and 90 min, following their penetration into the skin. As illustrated in Figure 3A, the CRO−DMNs initially exhibited a well-defined and intact pyramidal morphology prior to skin penetration. Gradual degradation at the tips was observed over time due to absorption by the skin, with significant deterioration occurring within 30 min. Subsequently, an HPLC analysis was conducted to determine the release profile of CRO, revealing complete release from CRO−DMNs within the aforementioned time frame (Figure 3B).

**3.4. CRO−DMNs Improve Cardiac Function and Reduce Infarct Size Resulting from MI.** To assess the impact of CRO−DMNs on cardiac function, echocardiography was performed to measure the ejection fraction (EF) immediately after MI (post) and again 28 days later (Figure 4A). Aside from the Sham group, the EF values of all MI mice including MI, DMNs, L-CRO+DMNs, H-CRO+DMNs, and CRO groups were significantly decreased immediately after MI induction, with no significant differences among them. This consistency indicates successful homogenization of the MI model. Excitingly, at 28 days post MI, the EF significantly increased in the L-CRO+DMNs, H-CRO+DMNs, and CRO groups compared to the MI group. Notably, the H-CRO+DMNs group exhibited the greatest improvement in EF, while no significant change was observed in the DMNs group. Furthermore, both L-CRO+DMNs and H-CRO+DMNs demonstrated a more substantial enhancement of EF compared with the CRO group (Figure 4B,4D). These results

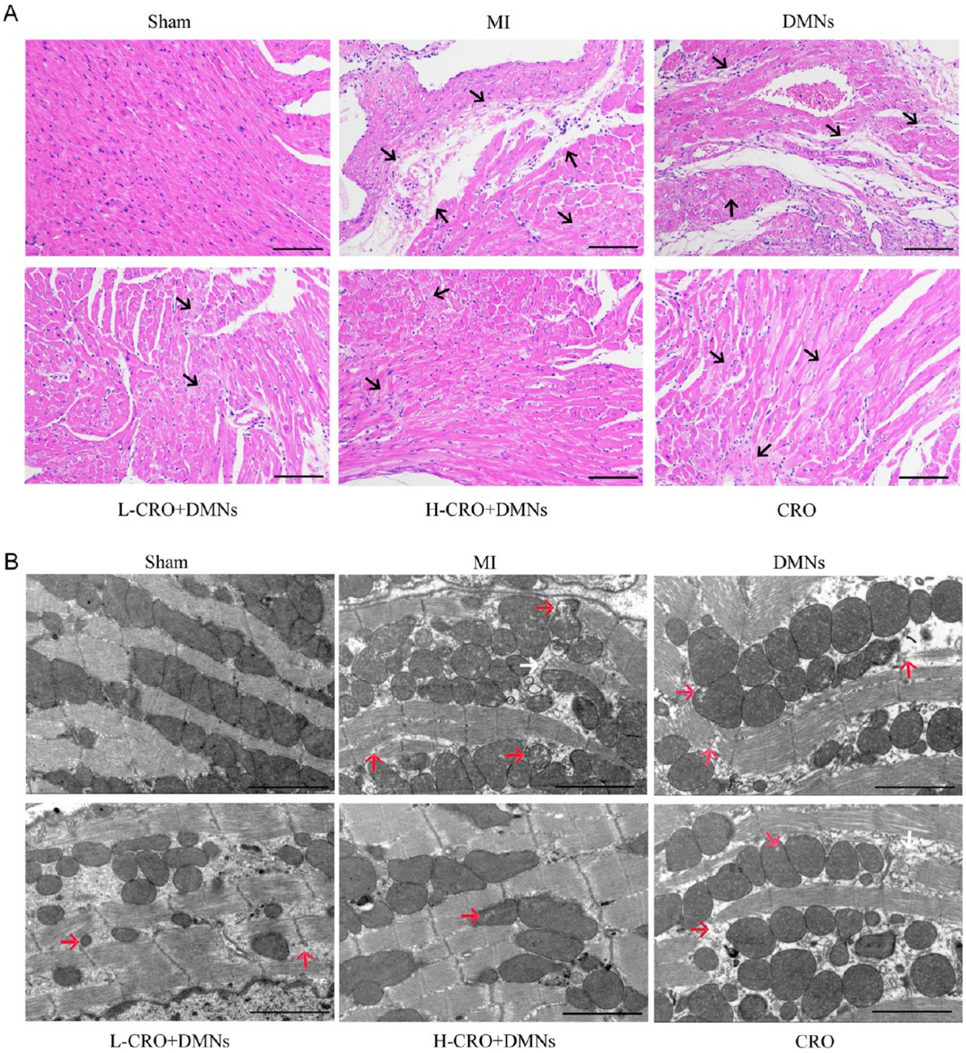

**Figure 5.** CRO−DMNs significantly improved myocardial tissue structure after myocardial infarction. (A) HE staining of myocardial tissue lesions (Bar = 100 μm). (B) TEM micrographs of myocardial tissues (Bar = 2 μm).

indicate that CRO−DMNs effectively improved cardiac function in post-MI hearts.

To investigate the effect of CRO−DMNs on cardiac fibrosis, we performed Masson's trichrome staining on infarcted hearts. Compared to the MI group, there was no statistical difference in the myocardial infarct area in the DMNs group. In contrast, significant reductions in the myocardial infarct area were evident in the L-CRO+DMNs, H-CRO+DMNs, and CRO groups, with the most pronounced effect observed in the H-CRO+DMNs group. Furthermore, both H-CRO+DMNs and L-CRO+DMNs groups exhibited superior improvement of the infarcted heart compared to the CRO group (Figure 4C,4E).

**3.5. CRO−DMNs Inhibited Myocardial Injury in Post-MI Hearts.** The histopathological changes in myocardial tissue were further evaluated by using HE staining. As shown in Figure 5A, the Sham group displayed normal myocardial structure with neatly arranged and tightly connected myocardial fibers. In contrast, significant histomorphological changes were observed in the MI group, including disruption of the myocardial cell structure in the infarcted area, massive infiltration of inflammatory cells, and lysis and rupture of myocardial fibers. By comparison, the L-CRO+DMNs and CRO groups exhibited reduced myocardial cell necrosis, while the H-CRO+DMNs group demonstrated minimal fiber breakage and inflammatory cell infiltration, closely resembling the structural characteristics of the Sham group. Conversely, the DMNs group displayed a structure similar to that of the MI group. These results suggested that DMNs enhance the therapeutic effect of CRO on myocardial injury after MI.

The ultrastructure of myocardial tissue was further examined by using transmission electron microscopy (TEM). The MI group revealed severe damage and rupture of myocardial tissue, disordered mitochondrial arrangement, disturbed internal cristae structure, and vacuole formation due to local expansion between the outer and inner membranes compared to the Sham group. In contrast, the CRO group showed a slight improvement in mitochondrial arrangement. Notably, both L-CRO+DMNs and H-CRO+DMNs groups exhibited more regular mitochondrial arrangement, complete internal cristae structure, significantly reduced vacuolization, and improved overall myocardial organization compared to the MI group. The H-CRO+DMNs group demonstrated the most pronounced enhancement effect (Figure 5B). These findings indicate that DMNs effectively enhance CRO's protective effects on myocardium and mitochondria.

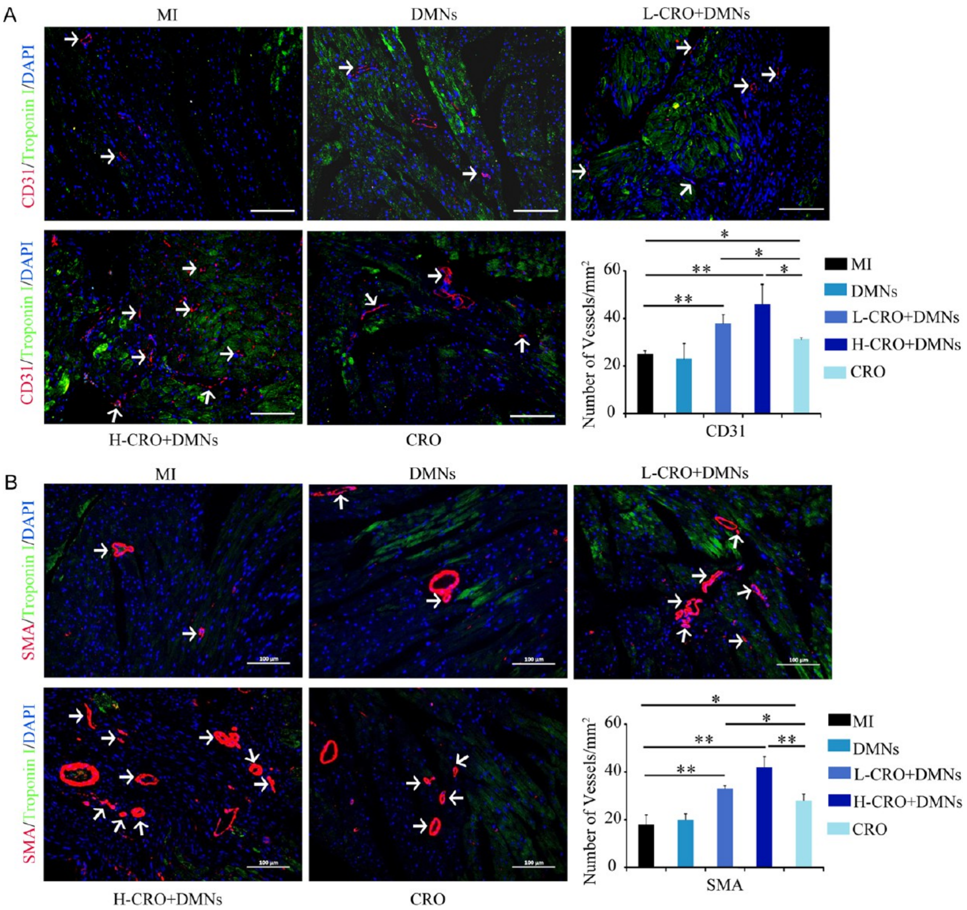

**Figure 6.** CRO−DMNs promote angiogenesis in post-MI hearts. (A) Images of CD31 immunofluorescence staining in each group 28 days after MI, along with statistical results, CD31 staining (red), troponin I staining (green), and DAPI staining (blue); (B) images of $\alpha$-SMA immunofluorescence staining in each group 28 days after MI, along with statistical results, $\alpha$-SMA staining (red), troponin I staining (green), and DAPI staining (blue). Bar = 100 $\mu$m. All data are presented as means ± SD $n = 5$ (number of animals/group), $^{*}P < 0.05$, $^{**}P < 0.01$ compared with the MI group.

**3.6. CRO−DMNs Promote Angiogenesis in Post-MI Hearts.** After MI, irreversible ischemia and hypoxia caused by blocked blood supply lead to the damage of cardiac cells. Vascular regeneration is essential to rescue ischemic myocardium and reverse ventricular remodeling. Therefore, immunofluorescent staining was performed using vascular smooth muscle cell marker $\alpha$-SMA and endothelial cell marker CD31 to assess arteriogenesis and angiogenesis in the peri-infarct myocardium, respectively.[40] As shown in Figure 6, compared with the MI group, the numbers of both CD31-positive and $\alpha$-SMA-positive vessels were significantly increased in the L-CRO+DMNs, H-CRO+DMNs, and CRO groups. Moreover, the L-CRO+DMNs and H-CRO+DMNs groups exhibited a further increase in the number of positive vessels compared to the CRO group, while there was no significant change between the DMNs and MI groups (Figure 6A,6B). These data suggested that DMNs significantly improved the angiogenic ability of CRO, thereby exerting anti-MI effects.

## 4. DISCUSSION AND CONCLUSIONS

Despite advances in medical technology, effective treatment options for MI remain limited to long-term pharmacotherapy and high-risk interventional procedures. Recently, CRO, the principal bioactive constituent of *Crocus sativus* (saffron), has garnered considerable attention due to its multifaceted pharmacological properties. Accumulating evidence has demonstrated that CRO possesses a wide range of beneficial properties, including anti-inflammatory, antidepressant, anti-tumor, neuroprotective, immunomodulatory, and hypotensive effects.[41] Although CRO may represent a promising therapeutic candidate for the treatment of myocardial infarction, its poor oral absorption and instability in the intestinal tract pose significant challenges to its clinical application.

Over the past few decades, microneedles, as a quintessential innovation in the realm of transdermal drug delivery, have garnered extensive application due to their unique advantages. These include painless self-administration, elimination of biohazardous sharp waste, and the capacity for controlled drug release.[25] Notably, clinical trials have been successfully conducted for the delivery of certain drugs and vaccines using microneedles, particularly DMNs.[42] The present study employed HA as the matrix material for DMNs, which is known for its safety and reliability. HA offers numerous advantages, including biodegradability within living organisms and nontoxicity to the human body.[43] Additionally, HA-based DMNs are nonreusable to minimize the risk of cross infection, leave no sharp residue after use, facilitate easier handling of medical waste, incur low cost, and reduce economic burden.[44] Importantly, they penetrate into shallower skin layers without causing pain, thereby improving patient compliance.[45]

Therefore, in our study, we incorporated HA as a matrix material to ensure biocompatibility, degradability, and mechanical strength sufficient to penetrate the stratum corneum. Our TEWL measurements demonstrated that microperforation induced by DMNs represents a noninvasive treatment approach with temporary and reversible puncture effects. Skin irritation studies revealed that the application of DMNs did not result in edema or erythema, indicating their excellent safety profile and biocompatibility. Then, we developed a CRO−DMN patch utilizing HA as a biodegradable matrix. Our results demonstrated that transdermal delivery of CRO via DMNs enhanced its efficacy in increasing infarct wall thickness and promoting cardiac function recovery in MI mice, indicating that our prototype CRO−DMNs offered a promising solution and opened up new avenues in MI therapy.

While our findings are promising, several limitations should be acknowledged. First, the study was conducted in a mouse model, and extrapolation to human physiology requires caution. Differences between species may influence drug absorption, distribution, metabolism, and overall efficacy. Therefore, further studies involving large animal models are warranted to validate the translatability of our results. Second, we did not extensively explore the underlying molecular mechanisms by which CRO exerts its cardioprotective effects. Investigating pathways related to angiogenesis, fibrosis inhibition, and mitochondrial preservation could provide deeper insights into the therapeutic action of CRO−DMNs. Lastly, the long-term safety and potential immunogenicity associated with repeated DMNs applications were not assessed and should be evaluated in future studies.

In a nutshell, we have successfully developed a safe and effective drug delivery system using HA-based DMNs for MI treatment by transdermal delivery of CRO. The CRO−DMNs not only overcome the limitations of CRO's poor oral bioavailability but also significantly enhance its therapeutic efficacy by improving cardiac function, promoting neovascularization, and inhibiting fibrosis in MI mice. This innovative approach holds substantial potential for clinical translation, offering a novel and patient-friendly therapeutic avenue for individuals suffering from MI and potentially other cardiovascular diseases. Future studies focusing on clinical trials and mechanistic explorations are essential to advance CRO−DMNs toward practical medical applications.

## ■ ASSOCIATED CONTENT

### Data Availability Statement

All data generated or analyzed during this study are included in this article (and its Supporting Information).

### Supporting Information

The Supporting Information is available free of charge at https://pubs.acs.org/doi/10.1021/acsomega.4c11540.

Morphological changes of DMN loaded with varying mass weights and the optical microscope images of different PF layers after insertion test using DMNs (PDF)

## ■ AUTHOR INFORMATION

### Corresponding Authors

**Liang Jin** − *School of Life Sciences, Zhejiang Chinese Medical University, Hangzhou, Zhejiang 310053, China; Shanghai Key Laboratory of Compound Chinese Medicines, The Ministry of Education Key Laboratory for Standardization of Chinese Medicines, Institute of Chinese Materia Medica, Shanghai University of Traditional Chinese Medicine, Shanghai 201203, China*; Email: liangjin881219@foxmail.com

**Ling Zhang** − *School of Life Sciences, Zhejiang Chinese Medical University, Hangzhou, Zhejiang 310053, China;* orcid.org/0000-0001-7542-1879; Email: zhanglingwws@163.com

### Authors

**Qian Liu** − *School of Pharmaceutical Science, Zhejiang Chinese Medical University, Hangzhou 310053, China; The First Affiliated Hospital of Zhejiang Chinese Medical University (Zhejiang Provincial Hospital of Chinese Medicine), Zhejiang Chinese Medical University, Hangzhou, Zhejiang 310006, China;* orcid.org/0000-0003-1437-3759

**Rui Zhao** − *School of Pharmaceutical Science, Zhejiang Chinese Medical University, Hangzhou 310053, China*

**Danni Zhang** − *School of Pharmaceutical Science, Zhejiang Chinese Medical University, Hangzhou 310053, China*

**Zhaohuan Lou** − *School of Pharmaceutical Science, Zhejiang Chinese Medical University, Hangzhou 310053, China*

**Jiangyue Wu** − *School of Pharmaceutical Science, Zhejiang Chinese Medical University, Hangzhou 310053, China*

**Shiying Hou** − *School of Pharmaceutical Science, Zhejiang Chinese Medical University, Hangzhou 310053, China*

**Bin Yang** − *School of Pharmaceutical Science, Zhejiang Chinese Medical University, Hangzhou 310053, China*

**Yunyun Lu** − *School of Pharmaceutical Science, Zhejiang Chinese Medical University, Hangzhou 310053, China*

**Mengyao Yuan** − *School of Pharmaceutical Science, Zhejiang Chinese Medical University, Hangzhou 310053, China*

**Shudong Lin** − *School of Life Sciences, Zhejiang Chinese Medical University, Hangzhou, Zhejiang 310053, China*

**Tianlei Wang** − *School of Engineering and Applied Science, University of Pennsylvania, Philadelphia 19104-6243 Pennsylvania, United States;* orcid.org/0009-0001-5633-5710

Complete contact information is available at:
https://pubs.acs.org/10.1021/acsomega.4c11540

### Author Contributions

[#]Q.L., R.Z., and D.N.Z. contributed equally to the work.

### Notes

The authors declare no competing financial interest.

## ■ ACKNOWLEDGMENTS

This work was supported by the grants from National Natural Science Foundation of China (No. 82173959, No. 82374110, No. 82304761, No. 81903830), the Natural Science Foundation of Zhejiang Province (No. LY23H280005), the Science and Technology Department of the State Administration of Traditional Chinese Medicine and the Zhejiang Provincial Administration of Traditional Chinese Medicine jointly build technology plan projects (No. GZY-ZJ-KJ-24065), Zhejiang Province Traditional Chinese Medicine Science and Technology project (No. 2023ZF157, No. 2023ZR080), the Research Project of Zhejiang Chinese Medical University (No. 2021RCZXZK23, No.

2022GJYY025, No. 2024JKZKTS25), and the Chinese funding program for postdoctoral researcher (No. GZC20231701).

## ■ REFERENCES

(1) Tsao, C. W.; Aday, A. W.; Almarzooq, Z. I.; Alonso, A.; Beaton, A. Z.; Bittencourt, M. S.; Boehme, A. K.; Buxton, A. E.; Carson, A. P.; Commodore-Mensah, Y.; et al. Heart Disease and Stroke Statistics-2022 Update: A Report From the American Heart Association. *Circulation* **2022**, *145* (8), e153−e639.

(2) Thygesen, K.; Alpert, J. S.; Jaffe, A. S.; Chaitman, B. R.; Bax, J. J.; Morrow, D. A.; White, H. D. Fourth Universal Definition of Myocardial Infarction (2018). *J. Am. Coll Cardiol.* **2018**, *72* (18), 2231−2264.

(3) Heusch, G.; Gersh, B. J. The pathophysiology of acute myocardial infarction and strategies of protection beyond reperfusion: a continual challenge. *Eur. Heart J.* **2017**, *38* (11), 774−784.

(4) Sobhani, Z.; Nami, S. R.; Emami, S. A.; Sahebkar, A.; Javadi, B. Medicinal Plants Targeting Cardiovascular Diseases in View of Avicenna. *Curr. Pharm. Des.* **2017**, *23* (17), 2428−2443.

(5) Shahi, T.; Assadpour, E.; Jafari, S. M. Main chemical compounds and pharmacological activities of stigmas and tepals of 'red gold'; saffron. *Trends Food Sci. Technol.* **2016**, *58*, 69−78.

(6) Efentakis, P.; Rizakou, A.; Christodoulou, E.; Chatzianastasiou, A.; López, M. G.; León, R.; Balafas, E.; Kadoglou, N. P. E.; Tseti, I.; Skaltsa, H.; et al. Saffron (Crocus sativus) intake provides nutritional preconditioning against myocardial ischemia-reperfusion injury in Wild Type and ApoE((−/−)) mice: Involvement of Nrf2 activation. *Nutr. Metab. Cardiovasc. Dis.* **2017**, *27* (10), 919−929.

(7) Yaribeygi, H.; Zare, V.; Butler, A. E.; Barreto, G. E.; Sahebkar, A. Antidiabetic potential of saffron and its active constituents. *J. Cell Physiol.* **2019**, *234* (6), 8610−8617.

(8) D'Onofrio, G.; Nabavi, S. M.; Sancarlo, D.; Greco, A.; Pieretti, S. Crocus Sativus L. (Saffron) in Alzheimer's Disease Treatment: Bioactive Effects on Cognitive Impairment. *Curr. Neuropharmacol.* **2021**, *19* (9), 1606−1616.

(9) Shafiee, M.; Aghili Moghaddam, N. S.; Nosrati, M.; Tousi, M.; Avan, A.; Ryzhikov, M.; Parizadeh, M. R.; Fiuji, H.; Rajabian, M.; Bahreyni, A.; et al. Saffron against Components of Metabolic Syndrome: Current Status and Prospective. *J. Agric. Food Chem.* **2017**, *65* (50), 10837−10843.

(10) Arzi, L.; Hoshyar, R. Saffron anti-metastatic properties, ancient spice novel application. *Crit Rev. Food Sci. Nutr.* **2022**, *62* (14), 3939−3950.

(11) Hashemzaei, M.; Mamoulakis, C.; Tsarouhas, K.; Georgiadis, G.; Lazopoulos, G.; Tsatsakis, A.; Shojaei Asrami, E.; Rezaee, R. Crocin: A fighter against inflammation and pain. *Food Chem. Toxicol.* **2020**, *143*, No. 111521.

(12) Yaribeygi, H.; Mohammadi, M. T.; Sahebkar, A. Crocin potentiates antioxidant defense system and improves oxidative damage in liver tissue in diabetic rats. *Biomed. Pharmacother.* **2018**, *98*, 333−337.

(13) Hussain, M. A.; Abogresha, N. M.; AbdelKader, G.; Hassan, R.; Abdelaziz, E. Z.; Greish, S. M. Antioxidant and Anti-Inflammatory Effects of Crocin Ameliorate Doxorubicin-Induced Nephrotoxicity in Rats. *Oxid Med. Cell Longev* **2021**, *2021*, No. 8841726.

(14) Oruc, S.; Gönül, Y.; Tunay, K.; Oruc, O. A.; Bozkurt, M. F.; Karavelioğlu, E.; Bağcıoğlu, E.; Coşkun, K. S.; Celik, S. The antioxidant and antiapoptotic effects of crocin pretreatment on global cerebral ischemia reperfusion injury induced by four vessels occlusion in rats. *Life Sci.* **2016**, *154*, 79−86.

(15) Morelli, S.; Salerno, S.; Piscioneri, A.; Tasselli, F.; Drioli, E.; De Bartolo, L. Neuronal membrane bioreactor as a tool for testing crocin neuroprotective effect in Alzheimer's disease. *Chem. Eng. J.* **2016**, *305*, 69−78.

(16) Tao, W.; Ruan, J.; Wu, R.; Zhao, M.; Zhao, T.; Qi, M.; Yau, S. S. Y.; Yao, G.; Zhang, H.; Hu, Y.; Chen, G. A natural carotenoid crocin exerts antidepressant action by promoting adult hippocampal neurogenesis through Wnt/$\beta$-catenin signaling. *J. Adv. Res.* **2023**, *43*, 219−231.

(17) Ragias, V.; Poutahidis, T.; Tsantarliotou, M.; Taitzoglou, I.; Donofrio, G.; Zervos, I.; Lavrentiadou, S. CROCIN MODULATES THE PLASMINOGEN ACTIVATOR (PA)/PA-INHIBITOR (PAI) SYSTEM AND ACCELERATES HEALING OF BLEOMYCIN-INDUCED PULMONARY INJURY IN RATS. *Chest* **2020**, *157* (6, Supplement), A151.

(18) Li, J.; Lei, H. T.; Cao, L.; Mi, Y. N.; Li, S.; Cao, Y. X. Crocin alleviates coronary atherosclerosis via inhibiting lipid synthesis and inducing M2 macrophage polarization. *Int. Immunopharmacol.* **2018**, *55*, 120−127.

(19) Badavi, M.; Mard, S. A.; Dianat, M.; Dashtbozorgi, N. Crocin attenuates oxidative stress and inflammation in myocardial infarction induced by isoprenaline via PPAR$\gamma$ activation in diabetic rats. *J. Diabetes Metab. Disord.* **2020**, *19* (2), 1517−1525.

(20) Wang, Y.; Wang, Q.; Yu, W.; Du, H. Crocin Attenuates Oxidative Stress and Myocardial Infarction Injury in Rats. *Int. Heart J.* **2018**, *59* (2), 387−393.

(21) Demir, M.; Altinoz, E.; Elbe, H.; Bicer, Y.; Yigitturk, G.; Karayakali, M.; Ballur, A. F. H. Effects of pinealectomy and crocin treatment on rats with isoproterenol-induced myocardial infarction. *Drug Chem. Toxicol.* **2022**, *45* (6), 2576−2585.

(22) Xi, L.; Qian, Z.; Du, P.; Fu, J. Pharmacokinetic properties of crocin (crocetin digentiobiose ester) following oral administration in rats. *Phytomedicine* **2007**, *14* (9), 633−636.

(23) Zhang, R.; Qian, Z.-Y.; Han, X.-Y.; Chen, Z.; Yan, J.-L.; Hamid, A. Comparison of the Effects of Crocetin and Crocin on Myocardial Injury in Rats. *Chin. J. Nat. Med.* **2009**, *7* (3), 223−227.

(24) Shakya, R.; Nepal, M. R.; Kang, M. J.; Jeong, T. C. Effects of Intestinal Microbiota on Pharmacokinetics of Crocin and Crocetin in Male Sprague-Dawley Rats. *Metabolites* **2020**, *10* (11), 424.

(25) Lee, H.; Song, C.; Baik, S.; Kim, D.; Hyeon, T.; Kim, D. H. Device-assisted transdermal drug delivery. *Adv. Drug Delivery Rev.* **2018**, *127*, 35−45.

(26) Yang, J.; Liu, X.; Fu, Y.; Song, Y. Recent advances of microneedles for biomedical applications: drug delivery and beyond. *Acta Pharm. Sin B* **2019**, *9* (3), 469−483.

(27) Sun, Y.; Liu, J.; Wang, H.; Li, S.; Pan, X.; Xu, B.; Yang, H.; Wu, Q.; Li, W.; Su, X.; et al. NIR Laser-Triggered Microneedle-Based Liquid Band-Aid for Wound Care. *Adv. Funct. Mater.* **2021**, *31* (29), No. 2100218.

(28) Zhang, X.; Chen, G.; Liu, Y.; Sun, L.; Sun, L.; Zhao, Y. Black Phosphorus-Loaded Separable Microneedles as Responsive Oxygen Delivery Carriers for Wound Healing. *ACS Nano* **2020**, *14* (5), 5901−5908.

(29) Wang, Z.; Yang, Z.; Jiang, J.; Shi, Z.; Mao, Y.; Qin, N.; Tao, T. H. Silk Microneedle Patch Capable of On-Demand Multidrug Delivery to the Brain for Glioblastoma Treatment. *Adv. Mater.* **2022**, *34* (1), No. e2106606.

(30) GhavamiNejad, A.; Li, J.; Lu, B.; Zhou, L.; Lam, L.; Giacca, A.; Wu, X. Y. Glucose-Responsive Composite Microneedle Patch for Hypoglycemia-Triggered Delivery of Native Glucagon. *Adv. Mater.* **2019**, *31* (30), No. e1901051.

(31) Shi, H.; Xue, T.; Yang, Y.; Jiang, C.; Huang, S.; Yang, Q.; Lei, D.; You, Z.; Jin, T.; Wu, F.; et al. Microneedle-mediated gene delivery for the treatment of ischemic myocardial disease. *Sci. Adv.* **2020**, *6* (25), No. eaaz3621.

(32) Zhang, X.; Chen, G.; Bian, F.; Cai, L.; Zhao, Y. Encoded Microneedle Arrays for Detection of Skin Interstitial Fluid Biomarkers. *Adv. Mater.* **2019**, *31* (37), No. e1902825.

(33) Wang, Z.; Luan, J.; Seth, A.; Liu, L.; You, M.; Gupta, P.; Rathi, P.; Wang, Y.; Cao, S.; Jiang, Q.; et al. Microneedle patch for the ultrasensitive quantification of protein biomarkers in interstitial fluid. *Nat. Biomed. Eng.* **2021**, *5* (1), 64−76.

(34) Sullivan, S. P.; Koutsonanos, D. G.; Del Pilar Martin, M.; Lee, J. W.; Zarnitsyn, V.; Choi, S. O.; Murthy, N.; Compans, R. W.; Skountzou, I.; Prausnitz, M. R. Dissolving polymer microneedle patches for influenza vaccination. *Nat. Med.* **2010**, *16* (8), 915−920.

(35) Sartawi, Z.; Blackshields, C.; Faisal, W. Dissolving microneedles: Applications and growing therapeutic potential. *J. Controlled Release* **2022**, *348*, 186−205.

(36) Saha, I.; Rai, V. K. Hyaluronic acid based microneedle array: Recent applications in drug delivery and cosmetology. *Carbohydr. Polym.* **2021**, *267*, No. 118168.

(37) Olatunji, O.; Das, D. B.; Garland, M. J.; Belaid, L.; Donnelly, R. F. Influence of array interspacing on the force required for successful microneedle skin penetration: theoretical and practical approaches. *J. Pharm. Sci.* **2013**, *102* (4), 1209−1221.

(38) Davis, S. P.; Landis, B. J.; Adams, Z. H.; Allen, M. G.; Prausnitz, M. R. Insertion of microneedles into skin: measurement and prediction of insertion force and needle fracture force. *J. Biomech.* **2004**, *37* (8), 1155−1163.

(39) Larrañeta, E.; Moore, J.; Vicente-Pérez, E. M.; González-Vázquez, P.; Lutton, R.; Woolfson, A. D.; Donnelly, R. F. A proposed model membrane and test method for microneedle insertion studies. *Int. J. Pharm.* **2014**, *472* (1−2), 65−73.

(40) Ahn, Y.; An, J. H.; Yang, H. J.; Lee, D. G.; Kim, J.; Koh, H.; Park, Y. H.; Song, B. S.; Sim, B. W.; Lee, H. J.; et al. Human Blood Vessel Organoids Penetrate Human Cerebral Organoids and Form a Vessel-Like System. *Cells* **2021**, *10* (8), 2036.

(41) Alavizadeh, S. H.; Hosseinzadeh, H. Bioactivity assessment and toxicity of crocin: a comprehensive review. *Food Chem. Toxicol.* **2014**, *64*, 65−80.

(42) Hirobe, S.; Azukizawa, H.; Hanafusa, T.; Matsuo, K.; Quan, Y. S.; Kamiyama, F.; Katayama, I.; Okada, N.; Nakagawa, S. Clinical study and stability assessment of a novel transcutaneous influenza vaccination using a dissolving microneedle patch. *Biomaterials* **2015**, *57*, 50−58.

(43) Lee, W. H.; Kim, W. Self-assembled hyaluronic acid nanoparticles for the topical treatment of inflammatory skin diseases: Beyond drug carriers. *J. Controlled Release* **2024**, *366*, 114−127.

(44) GhavamiNejad, P.; GhavamiNejad, A.; Zheng, H.; Dhingra, K.; Samarikhalaj, M.; Poudineh, M. A Conductive Hydrogel Microneedle-Based Assay Integrating PEDOT:PSS and Ag-Pt Nanoparticles for Real-Time, Enzyme-Less, and Electrochemical Sensing of Glucose. *Adv. Healthcare Mater.* **2023**, *12* (1), No. e2202362.

(45) Liu, J. F.; GhavamiNejad, A.; Lu, B.; Mirzaie, S.; Samarikhalaj, M.; Giacca, A.; Wu, X. Y. "Smart" Matrix Microneedle Patch Made of Self-Crosslinkable and Multifunctional Polymers for Delivering Insulin On-Demand. *Adv. Sci.* **2023**, *10* (30), No. e2303665.